

RESEARCH

Open Access



Long-term corrosion of copper alloys in the soil: new aspects of corrosion morphology in archaeological vessels from south-western Iran

Omid Oudbashi¹, Reza Naseri^{2*} and Parnia Asadi Hasanvand³

Abstract

A group of copper-based objects excavated at Deh Dumen cemetery, in south-western Iran, was studied and analysed to examine the long-term corrosion morphology and mechanism in the soil burial environment. For this purpose, twenty-two samples from twenty-one copper-based vessels were studied and analysed using X-ray diffraction, scanning electron microscopy—energy dispersive X-ray spectroscopy, micro-Raman spectroscopy and metallography techniques. The results of the analyses showed that the majority of vessels are made of tin bronze, along with two arsenical copper samples. The extent of corrosion observed ranges from very thin corrosion crusts to thick crusts and entirely corroded structures. These three identified corrosion morphologies display a multi-layered corrosion stratigraphy as well as the preserved limit of the original surface. The corrosion crusts include internal tin-rich and external copper-rich layers, and the main corrosion mechanism for the formation of multi-layered corrosion crusts is decuprification or selective dissolution of copper during the long-term burial time in a moderately Cl-contaminated soil. The three identified corrosion morphologies are similar to the previously published morphologies, but some clear deviations are apparent and are discussed here.

Keywords Archaeological tin bronze, Corrosion morphology, Decuprification, Original surface, Multianalytical approach

Introduction

Archaeological copper alloys, including tin bronze, brass, and arsenical copper, show variable morphological aspects of corrosion after long-term abandonment in burial environments such as soil and seawater [1–8]. These morphological aspects are strongly related to the

corrosive factors in the burial environment, although the metal/alloy composition and metallurgical characteristics also impact the corrosion mechanism and rate [3, 9–11]. The corrosion of archaeological copper alloys—and tin bronze, in particular—has been studied extensively during recent decades, and some typological morphologies and typical mechanisms have been identified and established [2, 12–15]. More recent studies revealed some new and interesting characteristics [16–21]. Therefore, it is necessary to continue investigation on excavated archaeological copper alloys to better understanding long-term corrosion mechanisms, and these results could also be useful for conservators.

Robbiola et al. suggested a model for corrosion morphology in archaeological tin bronzes buried in aerobic

*Correspondence:

Reza Naseri
reznaseri@uoaz.ac.ir

¹ Department of Conservation, University of Gothenburg, Medicinaregatan 7 B, 41390 Gothenburg, Sweden

² Department of Archaeology, University of Zabol, Bonjar Road, Zabol, Iran

³ Department of Conservation of Cultural and Historical Properties, Art University of Isfahan, Sangtarashha Alley, Hakim Nezami Street, Isfahan, Iran



© The Author(s) 2024. **Open Access** This article is licensed under a Creative Commons Attribution 4.0 International License, which permits use, sharing, adaptation, distribution and reproduction in any medium or format, as long as you give appropriate credit to the original author(s) and the source, provide a link to the Creative Commons licence, and indicate if changes were made. The images or other third party material in this article are included in the article's Creative Commons licence, unless indicated otherwise in a credit line to the material. If material is not included in the article's Creative Commons licence and your intended use is not permitted by statutory regulation or exceeds the permitted use, you will need to obtain permission directly from the copyright holder. To view a copy of this licence, visit <http://creativecommons.org/licenses/by/4.0/>. The Creative Commons Public Domain Dedication waiver (<http://creativecommons.org/publicdomain/zero/1.0/>) applies to the data made available in this article, unless otherwise stated in a credit line to the data.

burial environments in which two different corrosion morphologies form in single-phase α -tin bronzes according to the corrosivity of the soil environments [2]. This finding is based on the determination of the dissolution factor of alloy components and the presence or absence of the limit of the original surface within the corrosion layers. This classification explained the corrosion morphologies in archaeological bronzes, but some deviations were observed in other studies [3, 22]. Supplementary models of corrosion morphology and mechanism for archaeological tin bronzes have been presented elsewhere [17, 23, 24], focusing on wrought structure [17], but Robbiola's work has been the basis on which many hypotheses have been developed to understand bronze corrosion in the soil.

The presented research provides scientific analysis of corrosion morphology of archaeological tin bronze vessels excavated from Deh Dumen archaeological site, south-western Iran, and provides detailed documentation of the conservation condition in the metallic collections. The current work also introduces an update of knowledge concerning these issues based on analysis of some bronze (and arsenical copper) objects in order to interpret their corrosion morphology and places the obtained data in the context of previously published results. The aim of this paper is to understand the corrosion morphology in excavated and untreated archaeological vessels in the 2010s from the Bronze Age (ca. 3000–1500 BCE) of south-western Iran [25]. The results are compared with published corrosion profiles identified in bronze artefacts.

The ancient cemetery of Deh Dumen is located in south-western Iran, about 70 km north-west of the city of Yasuj, the capital of the Kohgiluyeh and Boyer-Ahmad province (34° 46' 84'' N, 51° 02' 99'' E) (Fig. 1a), partially encircling the Zagros fold and thrust belt chain [26]. The archaeological site is in the Khersan river valley on the western side of the river (Fig. 1b). The Deh Dumen cemetery is an important Iranian archaeological site due to its cultural and trade relationship between the western and eastern regions of the Iranian Plateau and the Indus valley, as evidenced by the presence of objects that are similar to those found in other sites [27–30]. Archaeological excavations in the cemetery of Deh Dumen have been carried out in four field campaigns from 2013 to 2023. The samples are taken from objects excavated in 2013 and 2019 (Table 1).

The vessels studied in this paper are excavated from the Deh Dumen Bronze Age cemetery in the Dena region, south-western Iran. Some experimental studies have been conducted on corrosion features of this site [31], but the current work is the first to investigate the corrosion morphologies comprehensively in these objects. Also, the

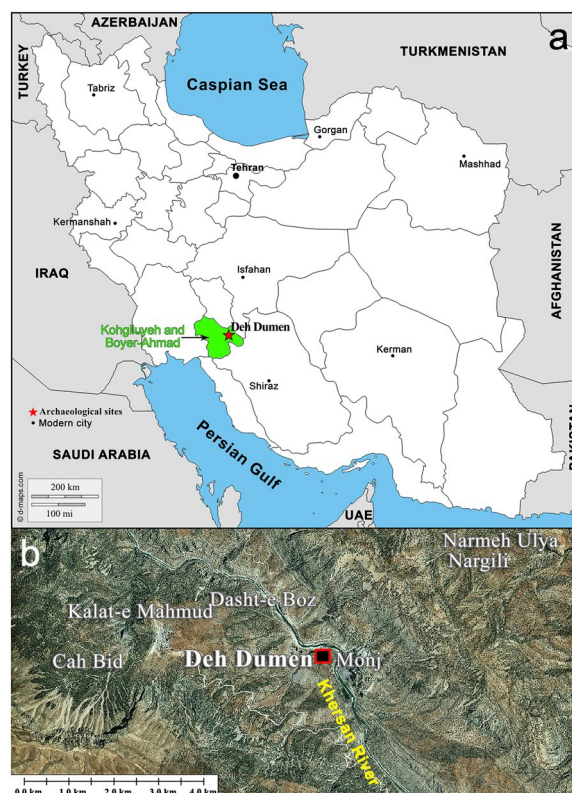


Fig. 1 a Map of Iran and location of Deh Dumen archaeological site in the Kohgiluyeh and Boyer Ahmad province, south-western Iran; b the location of the Deh Dumen site at the western side of the Khersan river

Deh Dumen bronze collection provides this opportunity to study the corrosion morphology in a well-documented large scale bronze collection from the Bronze Age of Iran. Therefore, study on corrosion morphology in this bronze collection can help conservators to understand the collection's condition, help them in conservation decision-making, and in developing a long-term preventive conservation approach for this bronze collection.

Materials and methods

Archaeological materials and sample preparation

To study the corrosion morphology of excavated bronzes from the Deh Dumen cemetery, twenty-two samples from twenty-one copper-based vessels excavated from 2013 to 2019 were selected (Fig. 2, Table 1). These investigated objects are different untreated, uncleaned, and unrestored vessels, stored in polyethylene bags and boxes after excavation and kept in an environment with relative humidity less than 50%, some of which have been analysed previously to characterize the microstructure, alloy composition and provenance studies [27, 28, 32]. The investigated objects include the vessels that were broken during burial and now are used for experimental analysis.

Table 1 Characteristics of twenty-two samples from twenty-one copper-based vessels from Deh Dumen, analysed in this research

Code	Excavation code	Object's type	Year of excavation	Corrosion status*	Conservation status
DD-01	DD-10027	Fragment of vessel	2019	Partially corroded	Broken and untreated
DD-02	DD-30-08	Tray	2019	Partially corroded	Broken and untreated
DD-03	DD-30-25	Fragmented vessel	2019	Partially corroded	Broken and untreated
DD-04	DD-31-02	Spouted vessel	2019	Partially corroded	Broken and untreated
DD-05	DD-31-06	Fragments of vessel	2019	Partially corroded	Broken and untreated
DD-06	DD-31-09	Base of vessel	2019	Partially corroded	Broken and untreated
DD-07	DD-31-10	Fragmented vessel	2019	Heavily corroded	Broken and untreated
DD-08	DD-31-29	Vessel	2019	Partially corroded	Untreated
DD-09	DD-31-39	Fragmented vessel	2019	Partially corroded	Broken and untreated
DD-10	DD-32-09	Vessel	2019	Partially corroded	untreated
DD-11	DD-32-10	Fragmented vessel	2019	Partially corroded	Broken and untreated
DD-12	DD-32-14	Vessel	2019	Partially corroded	untreated
DD-13	DD-34-05	Fragmented tray	2019	Partially corroded	Broken and untreated
DD-14	DD-36-08	Fragmented vessel	2019	Heavily corroded	Broken and untreated
DD-15	DP-102	Fragmented vessel	2013	Partially corroded	Broken and untreated
DD-16	DP-144	Fragmented vessel	2013	Partially corroded	Broken and untreated
DD-17	DP-150	Fragmented vessel	2013	Partially corroded	Broken and untreated
DD-18	DP-190-1	Base of vessel	2013	Partially corroded	Broken and untreated
DD-19	DP-190-2	Fragmented vessel	2013	Partially corroded	Broken and untreated
DD-20	DP-222	Fragmented vessel	2013	Heavily corroded	Broken and untreated
DD-21	DP-283	Vessel	2013	Partially corroded	Broken and untreated
DD-22	DP-287	Vessel	2013	Partially corroded	Broken and untreated

All analysed objects are untreated and studied after excavation in unrestored conditions

* Based on the cross-section observations

These broken objects were selected to facilitate the preparation of samples for experimental investigations. One small piece from each broken object was selected to perform analyses, and two samples were selected from vessel No. DP-190 (DD-18 and DD-19). Analysis of surface corrosion layers took place on a cross-section of each sample. The samples were embedded in epoxy resin and then ground by abrasive paper (240 to 5000 grid size). Finally, the cross-sections were polished with 3 and 1 μm diamond pastes.

Instrumentation

To study the corrosion morphology, the cross-sections were observed using optical microscopy (OM). For metallographic observations, a Zeiss Axio Imager M2m microscope, with 50 \times , 100 \times , 200 \times , 400 \times , and 500 \times magnifications, an AxioCam HRC digital camera, and AxioVision 4.X.X software were used. All cross-sections were observed in bright-field and dark-field illuminations.

The cross-sections were then studied and analysed by scanning electron microscopy-energy dispersive X-ray spectroscopy (SEM-EDS) technique. The microstructure and corrosion layers of the samples were observed

at different magnifications in the backscattered electron (BSE) mode. The chemical composition of the corrosion layers was detected using EDS analysis. The cross-sections were carbon-coated to make a conductive surface for SEM image preparation. Scanning electron microscopy-energy dispersive X-ray spectrometry analyses (SEM-EDS) were performed with a FE-SEM Zeiss Sigma HD equipped with an Oxford Instrument X-MaxN 80 SDD detector. Backscattered electron (BSE) images, EDS analysis, and X-ray mapping were conducted with an accelerating voltage of 20 kV in high vacuum, with a spot size of ~ 1 nm. The size of the analysed area for measurement of alloy composition was ca. 150 \times 150 microns and for the corrosion layers was based on the thickness of the layer.

Analysis of corrosion products was performed using X-ray Diffraction (XRD) technique. For this purpose, 0.5 g of surface corrosion products from all samples was removed mechanically by a scalpel and examined by XRD equipment, D8 ADVANCE model (Bruker, Germany), CuK α source with wavelength 1.54 \AA and 2θ between 5 $^\circ$ and 80 $^\circ$, at the Central Laboratory of the University of Isfahan, Iran. The X-ray diffractograms were characterized by using the Powder Diffraction File (PDF),

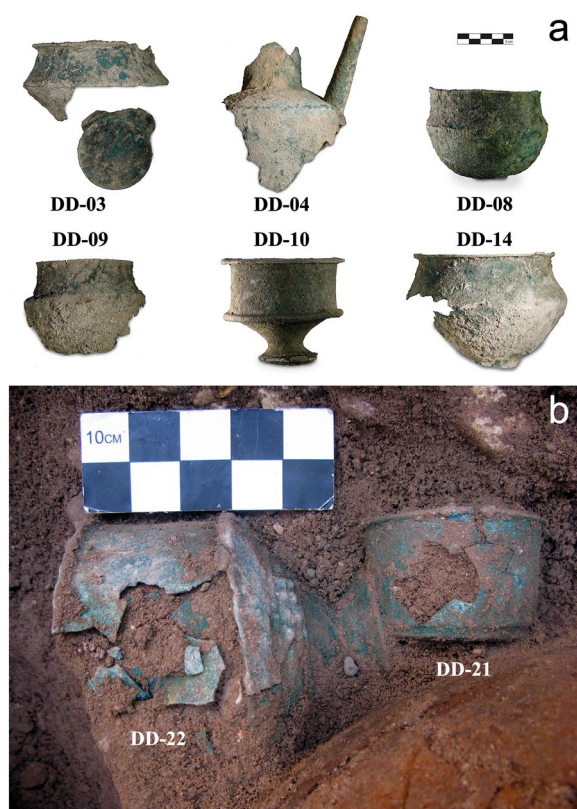


Fig. 2 a Some studied copper-based vessels from Deh Dumen; b two tin bronze vessels at the situation that they were discovered in burial site (DD-21 and DD-22) [28]

a database produced and maintained by the International Centre for Diffraction Data (ICDD[®]).

Raman analysis was performed on the corrosion layers of some selected samples using a Bruker Senterra spectrometer equipped with an Olympus 50× long working distance microscope objective and a charge-coupled device (CCD) detector. A Spectra Physics Cyan solid-state laser and a continuous wave diode laser emitting at 632 nm was used as the excitation source, and two holographic gratings (1800 and 1200 rulings/mm) provided a spectral resolution of 3–5 cm^{-1} . The output laser power was 20 mW, but the number of scans, and integration time were adjusted according to the Raman response of the different samples.

Results

Chemical analysis of core metal

The preliminary observation of the samples cross-section with optical microscopy revealed that objects could be classified into two different groups according to their corrosion layers: partially corroded objects with surface corrosion layers and significant amounts of metal under the corrosion layers (nineteen samples) and, completely

corroded objects in which no significant uncorroded metal is retained (three samples).

SEM–EDS analysis of the alloy composition of the first group of objects is presented in Table 2. Results are the average of three EDS analyses for each sample. Results showed that eighteen objects are made of binary tin bronze with tin content between ca. 7 and 12.5 wt% of tin. One sample displayed a different composition: the metal fragment inside the vessel's base (DD-18) is made of arsenical copper with 2.6 wt% of arsenic. The composition of the second group of objects was not calculated by SEM–EDS, but the semi-quantitative analytical data on the internal part of the cross-section showed that two objects are also made of tin bronze (DD-07 and DD-20) while DD-14 is likely made of arsenical copper.

Twenty vessels are made of tin bronze while one vessel and one vessel's base are made of arsenical copper (DD-14 and DD-18). These arsenical copper objects may have been produced due to smelting As-bearing copper ores, as was explained before in detail [28, 32]. It should be mentioned that the microstructure of all objects presented a single-phase solid solution of copper with no evidence of segregated high-tin phases or compounds.

Stratigraphy of corrosion layers

Eighteen partially corroded tin bronze objects show a complex corrosion crust including multiple distinct layers. The multi-layered corrosion structure in these tin bronze vessels shows two different morphologies. In the first morphology, a two-layered stratigraphy is observed in some bronze vessels (M1) in which the two main corrosion layers developed under the limit of the original surface (OS) (Fig. 3): layer A formed under the original surface as an almost uniform corrosion layer. It is very thin (20–50 μm) and dark-grey in colour. The original grain microstructure of bronze is retained as a pseudomorphic structure in this layer, and layer B formed between layer A and the alloy substrate, with very low thickness (<10 μm). It is more visible as an inter- or transgranular attack, red in colour. It should be noted that two additional very thin layers are observable in some samples as external corrosion crusts (Fig. 3): layer C is an irregular red corrosion layer formed over the original surface with a very low thickness. This layer does not cover the samples entirely and is not present in all samples of this morphology, and layer D is an irregular green corrosion layer formed over the original surface with a very low thickness. This layer does not cover the samples entirely and also is not present in all samples of this morphology.

In the second characterized morphology, the other bronze vessels display a more complex multi-layered corrosion (M2) in which four corrosion layers are

Table 2 Results of quantified SEM–EDS analysis of the alloy composition in nineteen partially corroded copper-based samples with remains of metal structure (wt%)

	S	σ	Fe	σ	Ni	σ	Cu	σ	Zn	σ	As	σ	Ag	σ	Sn	σ	Sb	σ	Pb	σ
DD-01	0.04	0.01	0.18	0.01	0.40	0.03	86.91	0.66	0.05	0.05	0.34	0.08			11.99	0.52				
DD-02			0.19	0.01	0.15	0.05	89.83	0.89			0.90	0.11	0.08	0.05	8.55	0.85	0.16	0.09	0.13	0.12
DD-03	0.04	0.02	0.14	0.03	0.32	0.04	89.41	0.27	0.06	0.05	0.64	0.04			9.26	0.29	0.07	0.06	0.04	0.05
DD-04	0.04	0.01	0.22	0.03	0.19	0.08	90.47	0.63	0.03	0.02	0.56	0.13			7.43	0.21	0.19	0.04	0.84	0.56
DD-05	0.07	0.06	0.18	0.01	0.18	0.06	91.04	0.34			0.48	0.02			7.15	0.44	0.02	0.02	0.85	0.54
DD-06			0.16	0.05	0.25	0.01	89.93	0.78	0.03	0.03	0.89	0.12	0.07	0.06	8.11	0.28	0.14	0.05	0.40	0.34
DD-08	0.04	0.04	0.22	0.02	0.20	0.12	88.60	0.07			0.21	0.09	0.03	0.03	10.24	0.13	0.17	0.08	0.26	0.04
DD-09	0.06	0.05	0.24	0.16	0.15	0.05	91.56	0.82	0.05	0.05	0.24	0.16	0.18	0.03	7.34	0.62	0.12	0.04	0.07	0.06
DD-10			0.11	0.03	0.06	0.06	90.18	0.64	0.07	0.05	0.43	0.13			9.03	0.67				
DD-11	0.01	0.00	0.17	0.03	0.01	0.01	87.94	0.81			0.31	0.10	0.25	0.03	11.13	0.74	0.08	0.02	0.08	0.07
DD-12	0.01	0.01	0.17	0.05	0.05	0.02	88.03	0.64			0.29	0.05	0.30	0.04	10.98	0.78			0.05	0.03
DD-13			0.03	0.02			91.18	0.43			0.29	0.06	0.19	0.05	8.11	0.42	0.10	0.09	0.04	0.04
DD-15			0.09	0.02	0.23	0.06	88.48	0.06	0.04	0.03	0.17	0.07	0.05	0.03	10.70	0.15	0.06	0.05	0.17	0.03
DD-16	0.03	0.01	0.08	0.00	0.21	0.04	88.29	0.28			0.17	0.15			10.95	0.26			0.21	0.10
DD-17	0.05	0.04	0.25	0.02	0.03	0.02	87.84	0.63			0.47	0.09	0.33	0.03	10.87	0.57	0.07	0.06	0.04	0.04
DD-18	0.08	0.03	0.66	0.04	0.28	0.03	95.72	0.32	0.07	0.06	2.60	0.21	0.20	0.06			0.16	0.10	0.19	0.09
DD-19	0.07	0.04	0.13	0.03			86.86	0.31	0.09	0.06	0.42	0.05			12.19	0.07			0.03	0.03
DD-21	0.14	0.10	0.40	0.03	0.23	0.07	88.64	0.20	0.09	0.09	0.66	0.06	0.02	0.02	9.50	0.10	0.18	0.15	0.13	0.04
DD-22	0.07	0.04	0.13	0.03			86.61	1.17			0.35	0.08			12.55	1.11	0.18	0.06		

Only sample DD-18 is made of arsenical copper while other samples are made of tin bronze. Results are the average of three EDS analyses for each sample. The bold values show amount of the main elements measured with EDS technique

well-developed under and over the limit of the original surface (Fig. 4): layer A formed under the original surface as an almost uniform, thick corrosion layer. It is variable in thickness (20–200 μm), varied in colour from dark-grey to red and orange in different samples. The original grain microstructure of bronze is retained as a pseudo-morphic structure in this layer. layer B is formed between layer A and the alloy substrate. Layer B is variable in thickness, red in colour, and more visible as an inter- or transgranular attack revealing the twin bands and slip lines and the grain structure of the bronze matrix, sometimes covering significant parts of the metal substrate, layer C formed over the original surface, red in colour and low in thickness (20–200 μm), and layer D formed over Layer C as the outermost corrosion layer. It is green in colour and sometimes is mixed with soil particles. Its thickness is variable in different samples and also within areas of the same sample (10–500 μm). This layer is also covered with a thin layer of soil contamination.

Layer B observed in both corrosion morphologies introduced above, mostly includes inter- or transgranular attacks and, in fact, resembles localized corrosion. This thin red (or orange) layer represents the early stages of corrosion/oxidation/dissolution of copper caused by a corrosive solution penetrating into the metal through the crack. If this becomes extensive, this localized corrosion

may result in cracking and embrittlement of archaeological tin bronzes, especially if they retain large amounts of deformation in the microstructure due to thermo-mechanical operations [33, 34], as has been identified before in Deh Dumen vessels [28, 31, 32].

As mentioned above, three vessels showed a heavily corroded microstructure in which the metal substrate is not visible in the cross-section of the sample. These vessels also include multiple corrosion layers, although the limit of the original surface is retained between the corrosion crust. The distinct layers observed in these objects include (Fig. 5): layer A formed as an almost uniform layer under the original surface. It is red or dark-red in colour and its thickness is between 100 and 200 μm in samples DD-07 and DD-20. In sample DD-14, this layer covered all parts of the internal layer below the original surface, layer B is green in sample DD-07 and DD-20 and covered almost all internal parts of the object below layer A, although sometimes some islands of the dark red corrosion product are visible in this thick internal matrix. This is not observed in sample DD-14 as a uniform layer, but rather some green islands are scattered in the internal red matrix of this sample, layer C formed over the original surface as an almost uniform dark red corrosion layer with 50–100 μm thickness, and layer D is a green layer covering the layer C. It is the outermost corrosion layer,

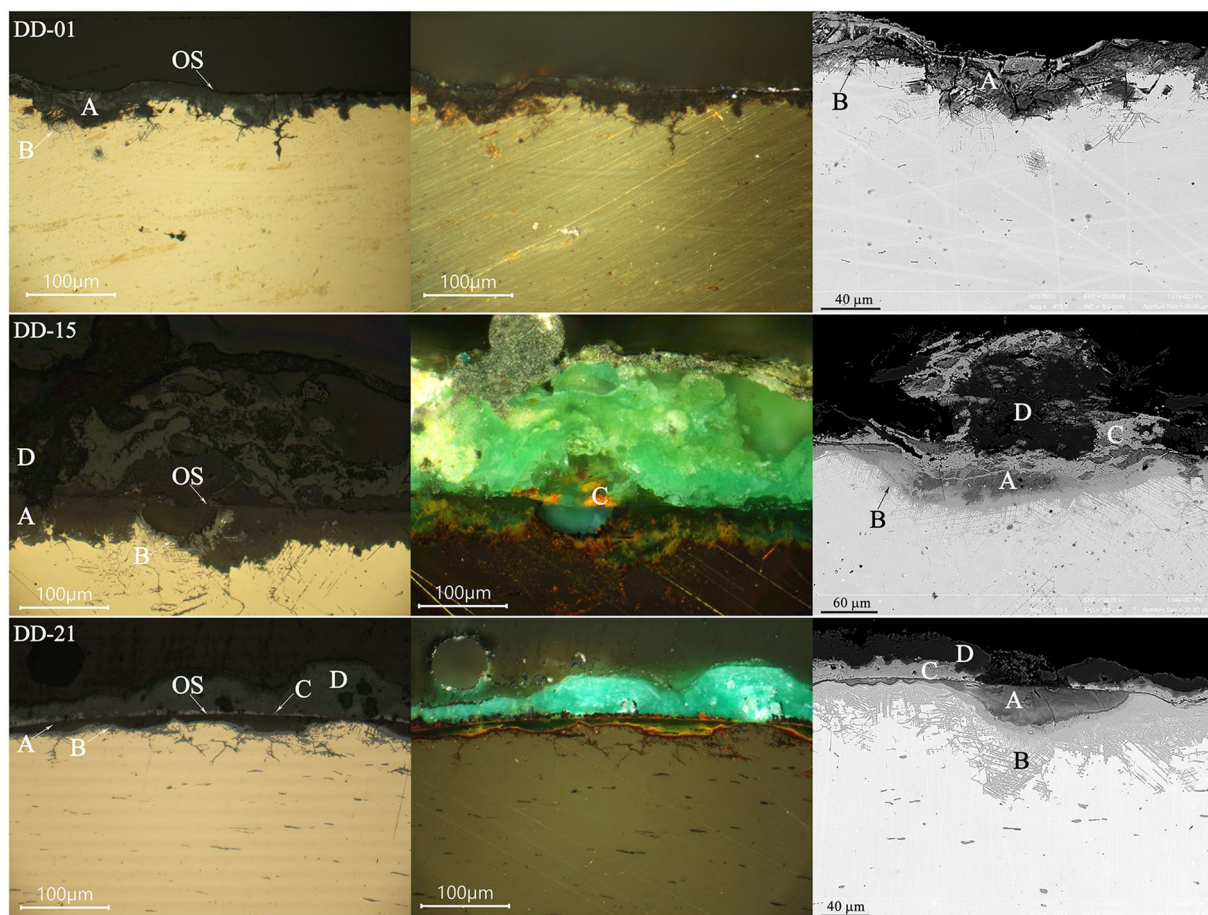


Fig. 3 Optical and SEM-BSE micrographs of three samples of the M1 morphology with very thin internal smooth patina (layers A and B) and some thin external corrosion layers (C and D). The limit of the original surface (OS) is obviously visible

though it is sometimes covered with a soil contamination layer. Its thickness is variable from 50 to 200 μm.

The only arsenical copper sample with metal residue (DD-18) also shows a partially multi-layered corrosion microstructure similar to most of the tin bronze vessels, although in contrast, external red and green layers (C and D) are mixed in many areas and layer B is not visible similar to tin bronze vessels despite some very small corrosion attacks that are visible below Layer A. However, it should be mentioned that the corrosion crust of this Cu-As object could be classified as a four-layered corrosion morphology as follows (Fig. 5): layer A formed under the original surface in dark-red to dark-brown colour. Its thickness is variable from 50 to 300 μm in different areas of the object, while some very tiny intergranular attacks are formed under this layer, layer B formed as some local red–orange attacks under layer A, layer C formed as a non-uniform corrosion layer over the original surface and with very low thickness (10–20 μm) with some thicker projections, layer D covered the original surface

and is green in colour with numerous islands of dark-red corrosion phase. Its thickness is significant and sometimes reaches 400–500 μm.

The two internal layers (A and B) are common in both M1 and M2 morphologies of tin bronze vessels, although their thickness is different. Figure 6 shows SEM-BSE micrographs of samples from different morphologies in higher magnifications in which the internal corrosion layers (A and B) show pseudomorphic replacement of the alpha matrix with the corrosion products. In fact, the ghost microstructure of the bronze matrix including worked and annealed grains is well-preserved in the internal corrosion layers due to long-term corrosion processes in the burial environment, as also observed previously in corroded bronze objects [3, 12, 22, 24, 35–38]. This ghost microstructure can be deduced only in the internal corrosion layers under the limit of the original surface and is very helpful to characterize the original surface's limit [39], while the extensive inter- and transgranular attacks (Layer B) could be visible in the alloy/

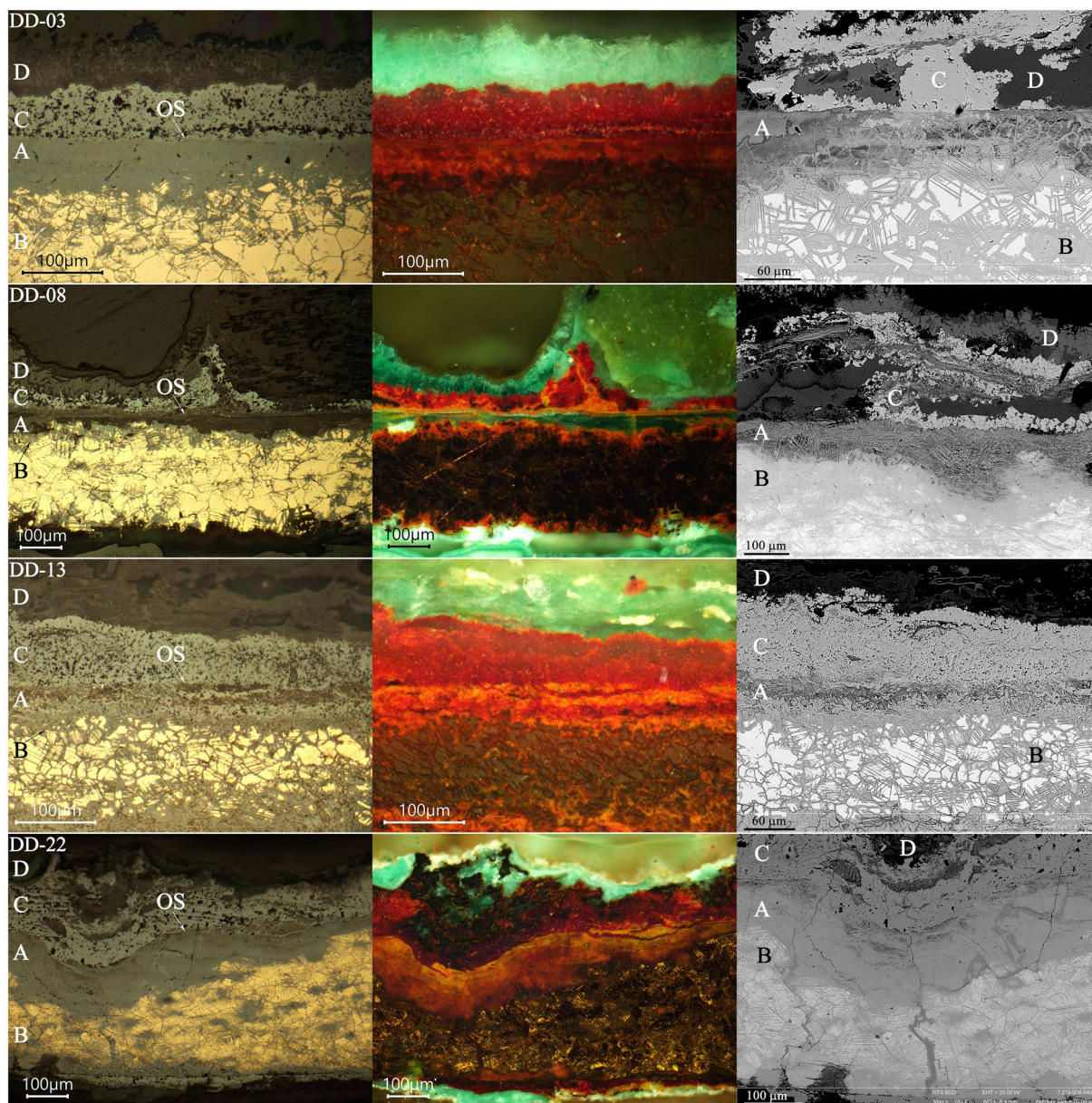


Fig. 4 Optical and SEM-BSE micrographs of four samples of the M2 morphology with thick internal corrosion layers (A and B) and thick external corrosion layers (C and D). The limit of the original surface (OS) is obviously visible

corrosion interface of the M1 and M2 morphologies, as the results of corrosion penetration.

Results of semi-quantitative EDS analysis as well as elemental EDS mapping of partially corroded morphologies (Fig. 7, DD-03) showed that in M1 and M2 morphologies, layer A is tin-rich and has a lower Cu/Sn ratio in comparison with bronze matrix, and some evidence of the metallurgical characteristics of the original metal, such as pseudomorphic retention of the microstructure and elongated inclusions [17], are

visible in the layer structure. It is worth noting that these inclusions are previously analysed and are composed of copper sulphide [28, 32]. Layer B, or the inner part of the internal crust, has a red/brown colour and an elemental composition containing Cu, Sn and O and a much higher Cu/Sn ratio than Layer A. The external layers are more commonly observed in the tin bronze vessels with M2 morphology, and their EDS analysis also showed that they are composed of copper with

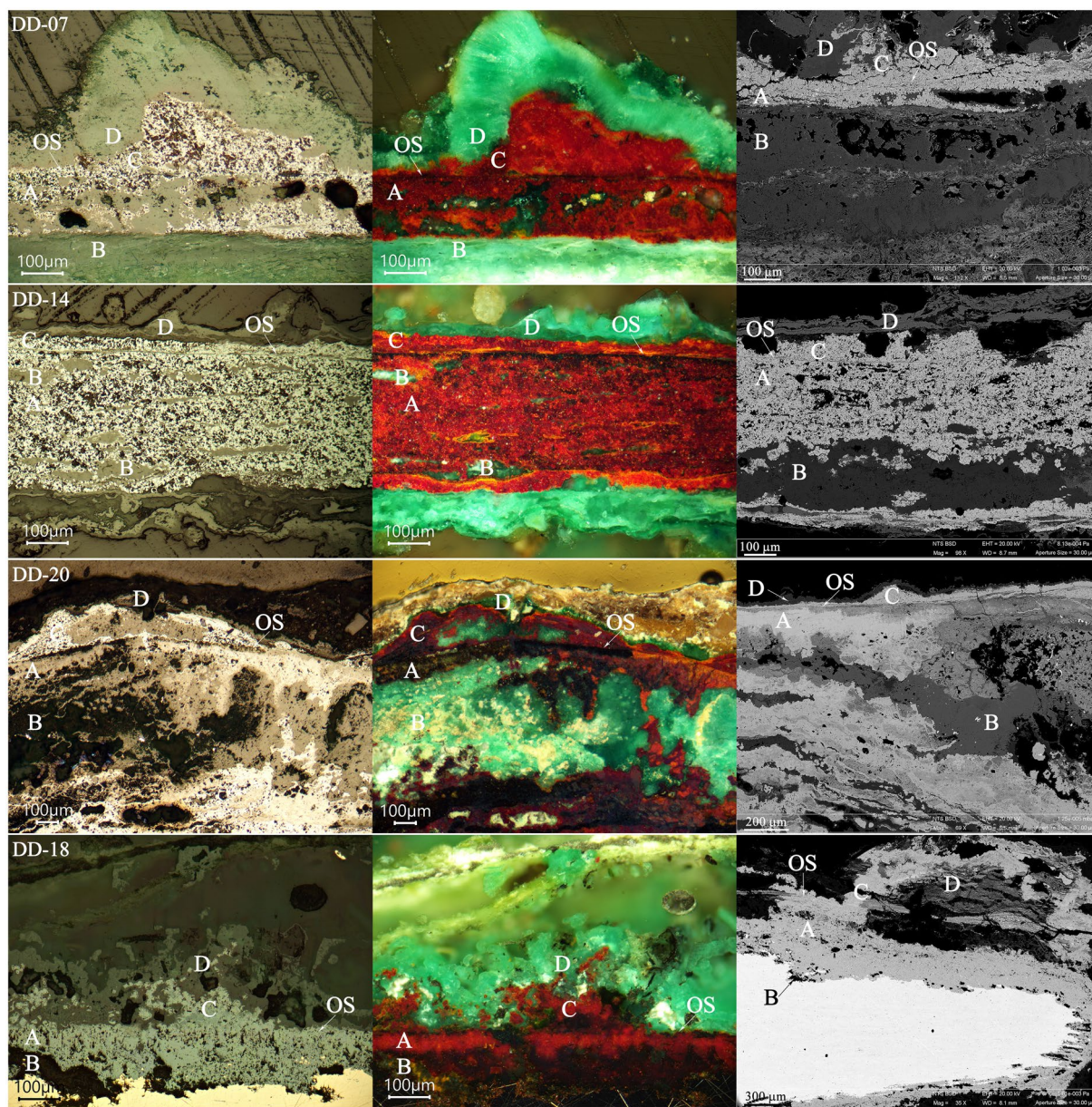


Fig. 5 Optical and SEM-BSE micrographs of three samples of the completely corroded M3 morphology, DD-07, DD-14 and DD-20, with internal corrosion layers (A and B) and thick external corrosion layers (C and D). The micrographs of the arsenical copper sample (DD-18) are very similar to M2 morphology. The limit of the original surface (OS) is obviously visible

variable amounts of oxygen, as observed in sample DD-03. Furthermore, the elemental EDS mapping of an entirely corroded sample from M3 morphology (DD-20) showed high concentrations of copper and tin in the internal layers, while some copper- and chlorine-rich corrosion products with almost no tin are formed within the internal layers. The external corrosion layers

(C and D) are similar to other morphologies from a chemical viewpoint.

Mineralogy of corrosion products

X-ray diffraction

Analysis of corrosion products of the vessels revealed a variety of copper corrosion products and soil minerals (Table 3 and Fig. 8). Cuprite (Cu_2O) was detected

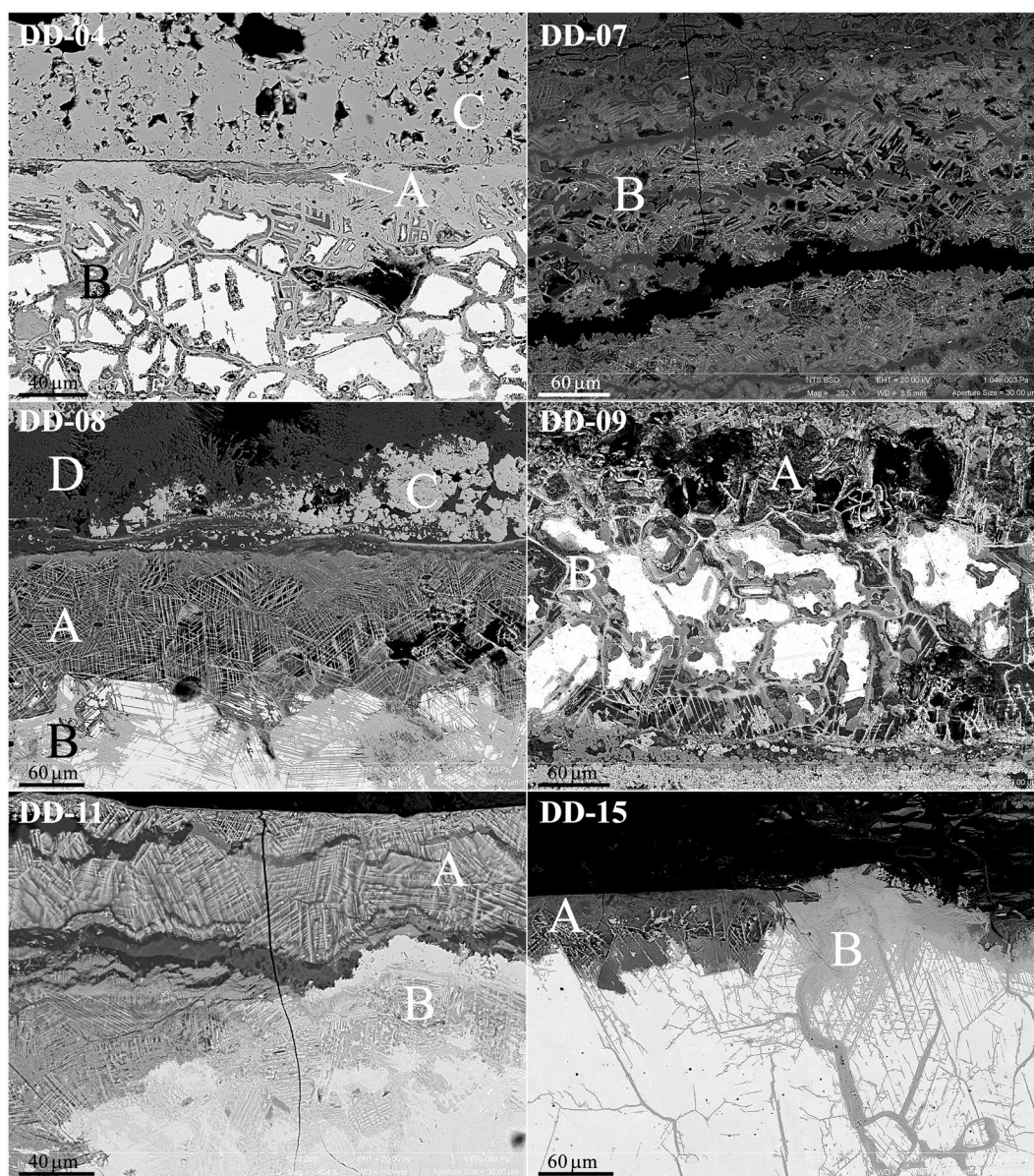


Fig. 6 SEM-BSE micrographs of some details of the microstructure of the corrosion layers including the pseudomorphic replacement (ghost structure) formed in the internal corrosion layers (A and B)

as the major corrosion product in all samples while malachite ($\text{Cu}_2\text{CO}_3(\text{OH})_2$) was identified as the major and minor product in all samples (except for sample DD-01). Tenorite (CuO) and copper trihydroxychlorides ($\text{Cu}_2(\text{OH})_3\text{Cl}$) were also found as minor phases in the majority of analysed samples. Cuprite and malachite are typical corrosion products in buried copper alloys, and they are formed together in corrosion layers of archaeological objects in moderately corrosive soils, in the presence of high moisture and CO_2 content. In fact, cuprite is the first product of copper oxidation in soil, but in

slightly alkaline soils, bronze will develop a green layer of malachite [40–42]. The presence of tenorite is an interesting aspect of corrosion in the Deh Dumen copper-based objects, as this copper oxide mineral forms in very specific conditions, including high temperature, high pH environment or high concentration of oxygen [40]. Nevertheless, it shows that the pH may have been alkaline in the burial environment (as is measured before about 8 [31]), or the concentration of oxygen may have been fluctuated during the long-term burial of the metal objects, as also has been observed in another copper-based

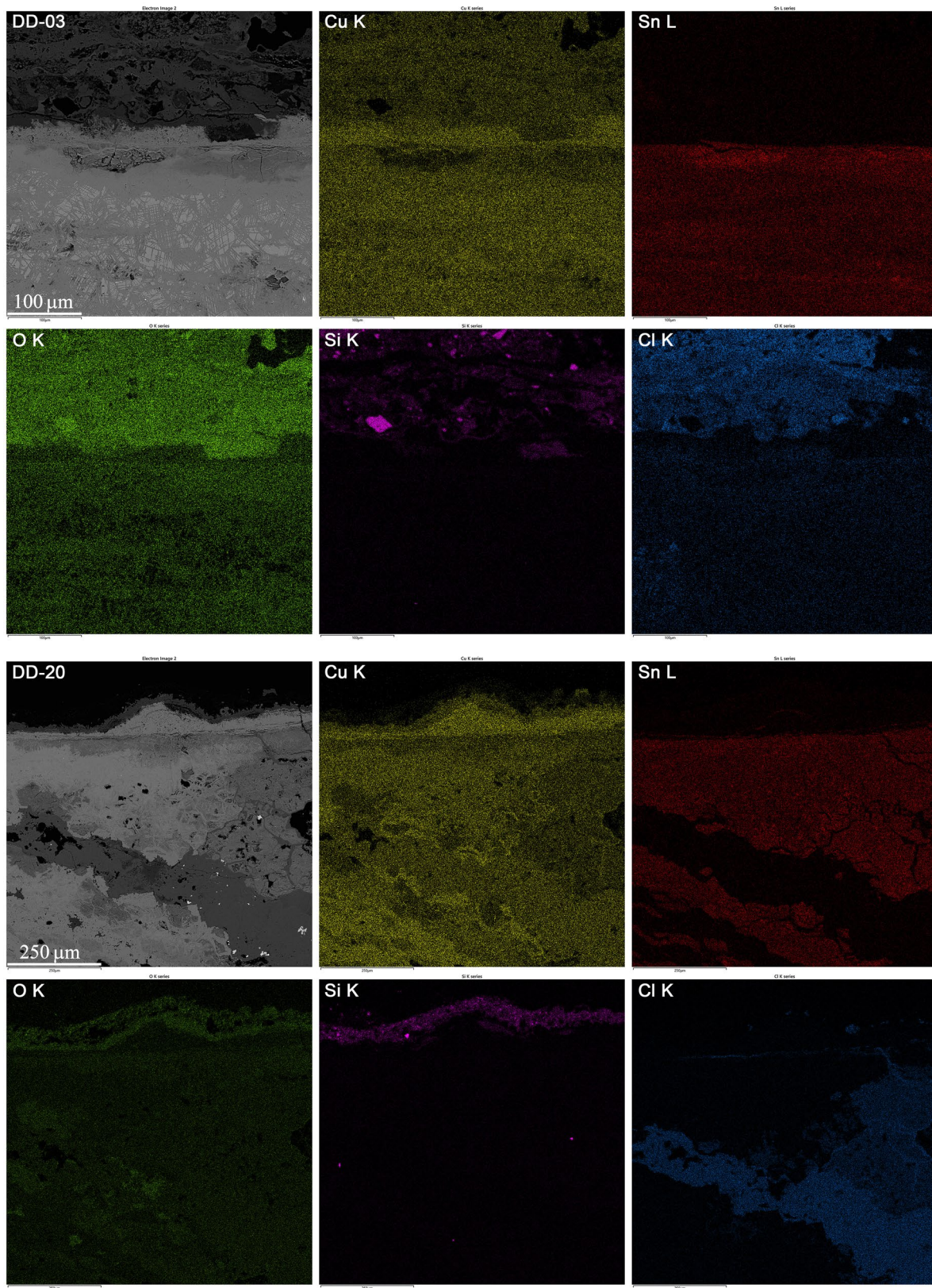


Fig. 7 EDS elemental map of the corrosion layers in two corroded tin bronze samples showing the different Cu/Sn proportion in the internal corrosion layer and the metal parts in sample DD-03 and presence of chloride corrosion product in internal part of sample DD-20

Table 3 Results of XRD analysis of corrosion layers in twenty-two samples from twenty-one copper-based vessels from Deh Dumen; XXX: major phase, XX: minor phase, X: trace phase

	Cuprite Cu ₂ O	Tenorite CuO	Malachite Cu ₂ CO ₃ (OH) ₂	Paratacamite Cu ₂ (OH) ₃ Cl	Atacamite Cu ₂ (OH) ₃ Cl	Brochantite Cu ₄ SO ₄ (OH) ₆	Copper Cu	Quartz SiO ₂	Calcite CaCO ₃
DD-01	XXX	XX							
DD-02	XXX	X	X		XX			X	
DD-03	XXX	X	XX		X		XX	X	X
DD-04	XXX	X	XX	X	X		XX		
DD-05	XXX	X	XX	X	X		XX	X	
DD-06	XXX	X	XX	X	X		XX	X	
DD-07	XXX	X	XX	X	X		XX	X	XX
DD-08	XXX	X	XX	X	XX		XX	XX	X
DD-09	XXX	X	XX	X	X		X	X	
DD-10	XXX	X	X		XX		XX	X	
DD-11	XXX	X	XX	X	X		X		X
DD-12	XXX		XX		X				
DD-13	XXX		XXX	X	X			X	XX
DD-14	XXX	X	XX	X	X		X		X
DD-15	XXX	X	XX				XX		X
DD-16	XXX		XX					XX	XX
DD-17	XXX		XX				X	XX	
DD-18	XXX		XXX						
DD-19	XXX		XXX						
DD-20	XXX	X	XX	X	X	X	X	X	
DD-21	XXX	X	XX					X	
DD-22	XXX	X	XX	X	X				

collection from Iran and other regions [3, 43, 44]. An isomer of malachite, azurite (Cu₃(CO₃)₂(OH)₂), is a more rare corrosion product on copper and bronze objects in soil, and its formation strongly depends on the presence of environments rich in moisture and bicarbonate anion (HCO₃⁻) [45, 46].

Copper trihydroxychlorides, or basic copper chlorides, are another group of corrosion products commonplace in archaeological copper alloys. The presence of chloride ions in burial environments may lead to the formation of nantokite (CuCl). During burial or after excavation, nantokite will form atacamite or paratacamite in the presence of moisture and oxygen. This so-called phenomenon "bronze disease" or "active corrosion" is a cyclic reaction that can take place in the presence of oxygen or chlorine ions, and the reaction will continue until all copper is transformed into copper corrosion products [40, 47–49]. This event is actually the reaction of copper with chlorine in the presence of moisture and oxygen that causes the formation of copper trihydroxychlorides (e.g., atacamite, paratacamite) and will continue in the presence of moisture [40, 50].

Brochantite (Cu₄SO₄(OH)₆) was detected as a minor corrosion product in one sample (DD-20). Basic copper

sulphates (including brochantite) are rare corrosion products in buried copper-based objects and have been observed as the main corrosion products in metal monuments exposed to urban environments [40, 51, 52]. Brochantite has also been observed as a corrosion product in some archaeological bronzes and has been attributed to the oxidation of copper sulphides which result from bacterial activities in the burial environment [53], or from high concentrations of soluble sulphate anion in the burial environment [3].

Copper is also detected as a minor phase in a significant number of samples. It may be introduced from the metallic substrate under the corrosion layers that has been mixed with the samples during mechanically removing the corrosion crusts for XRD analysis.

Micro-Raman spectroscopy

Raman spectra of four different layers in mounted cross-section (before carbon coating) from five objects of M1 and M2 morphologies are presented in Fig. 9. Table 4 also presents the peaks and identified phases in the different layers. The Raman spectra of layer A in three samples (DD-01, DD-08 and DD-15) show notably weak Raman peaks. In fact, layer A demonstrates no specific peak in

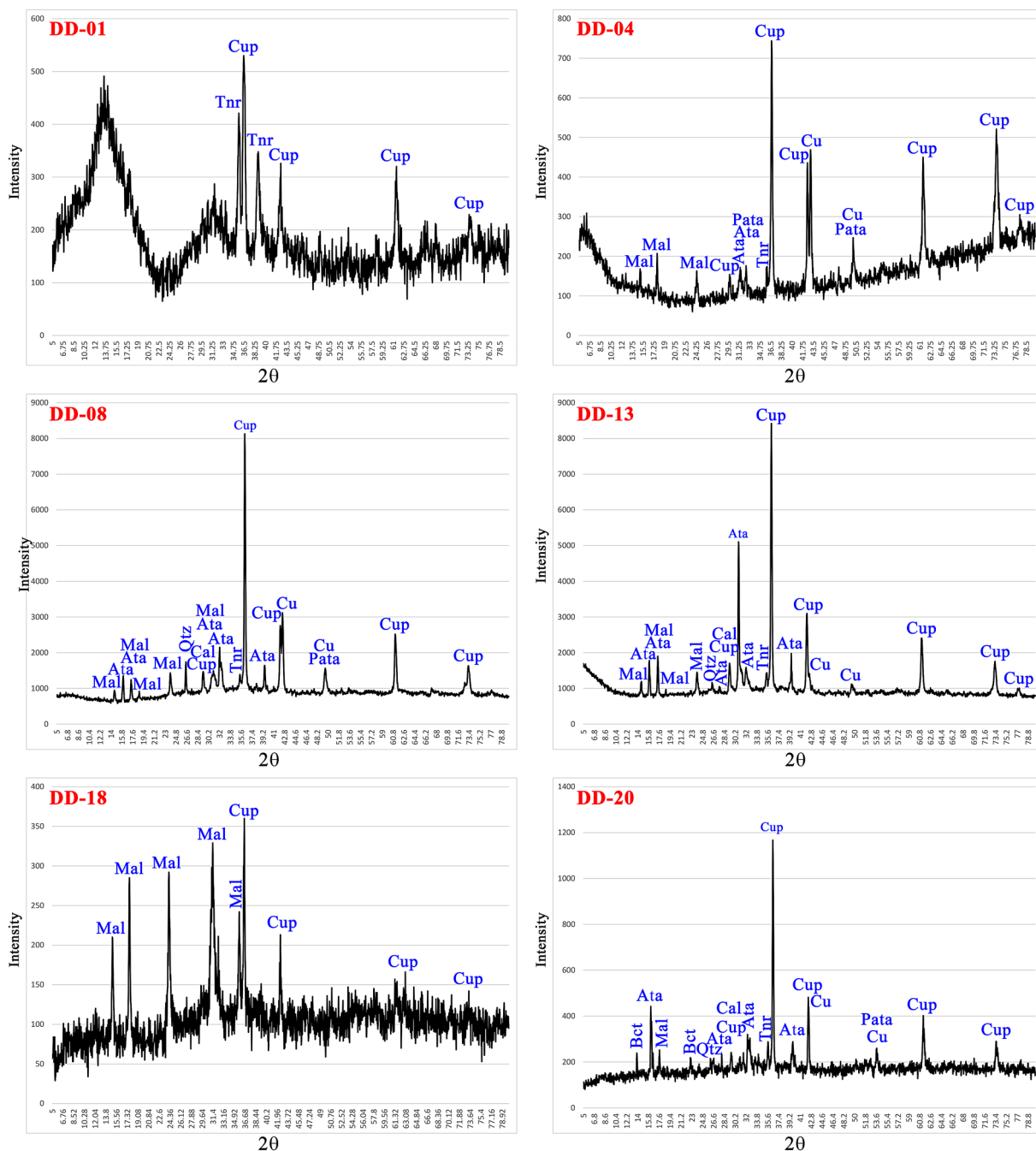


Fig. 8 X-ray diffractogram of corrosion products of some samples from Deh Dumen; *Cup* cuprite, *Tnr* tenorite, *Mal* malachite, *Ata* atacamite, *Pata* paratacamite, *Cu* copper, *Bct* brochantite, *Qtz* quartz, *Cal* calcite

sample DD-01, while some partially intensive peaks are visible in 84 and ~270 cm^{-1} in two other samples (DD-08 and DD-15). Additionally, one weak Raman peak at 620 cm^{-1} in sample DD-08 corresponds to cassiterite (SnO_2) [54, 55]. This tin oxide compound forms more as an amorphous or non-crystalline corrosion product in the internal corrosion layer of tin bronzes and it is

not easy to detect through techniques such as XRD, but μ -Raman is a helpful technique to find traces of cassiterite [10]. Layer B analysed in three samples (DD-03, DD-08, DD-13) shows very similar Raman spectra with intense peaks at 148, 220 and 624 cm^{-1} that correspond to cuprite, although a peak is also observed in 308 cm^{-1} in sample DD-08 that can be attributed to tenorite

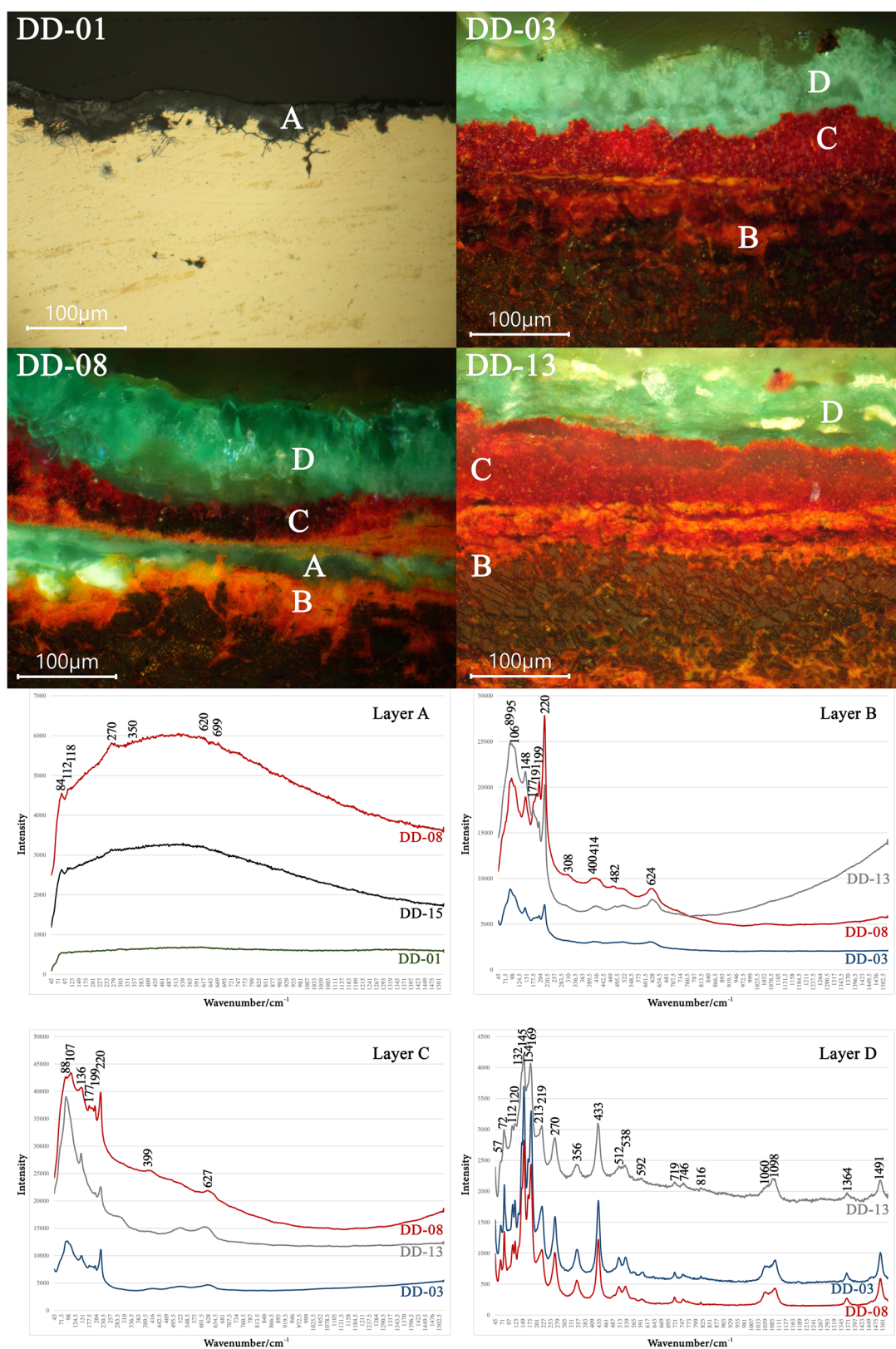


Fig. 9 μ -Raman spectra of four different corrosion layers (A, B, C and D) observed in some selected samples from M1 and M2 morphologies

Table 4 Results of μ -Raman analysis on different corrosion layers in some copper-based vessels from Deh Dumen. The bold values are the main Raman peaks corresponding to the identified corrosion products

Sample	Layer	Raman peaks	Corrosion product	References
DD-01	A	No clear peak	Not identified	–
DD-03	B	90, 106, 148 , 177, 191, 199, 220 , 624	Cuprite	[56–58]
	C	88, 95, 106, 137 , 177, 199, 221	Cuprite	[56–58]
	D	57, 74, 114, 120 , 132, 147 , 154, 173 , 215, 219, 272 , 356, 436 , 512, 538, 596, 719, 743, 817, 1060, 1096 , 1362, 1491	Malachite, Paratacamite/Atacamite	[59–63]
DD-08	A	84 , 112, 118, 270 , 350, 620, 699	Cassiterite	[54, 55]
	B	89, 95, 106, 148 , 177, 191, 199, 220 , 308, 400, 414, 482, 624	Cuprite, tenorite	[56–58]
	C	88, 107, 136 , 177, 199, 220 , 399, 627	Cuprite	[56–58]
	D	57, 74, 114, 120 , 132, 148 , 154, 173 , 220, 270 , 356, 433 , 512, 538, 595, 719, 744, 816, 1060, 1095 , 1362, 1491	Malachite, Paratacamite/Atacamite	[59–63]
DD-13	B	89, 95, 106, 148, 177 , 199, 220 , 400, 414, 482, 624	Cuprite	[56–58]
	C	88, 136 , 199, 220 , 399, 520, 627	Cuprite	[56–58]
	D	57, 72 , 112, 120, 132, 145 , 154, 169 , 213, 219, 270 , 356, 433 , 512, 538, 592, 719, 746, 816, 1060, 1098 , 1364, 1491	Malachite, Paratacamite/Atacamite	[59–63]
DD-14	A	89, 94, 147 , 177, 199, 220 , 296, 418, 522, 623	Cuprite, tenorite	[56–58]
	B	79, 83, 111, 118, 145 , 180 , 219, 270 , 355, 434 , 1366, 1491	Malachite	[59–61]
	C	89, 94, 148 , 177, 199, 220 , 296, 418, 623	Cuprite, Tenorite	[56–58]
	D	75, 83, 95, 119 , 143, 149 , 174, 279, 402, 443 , 515, 893, 1001	Malachite, Paratacamite/Atacamite	[59–63]
DD-15	A	84 , 113, 117, 267	Not identified	–
DD-18	A	90, 99, 148 , 178, 199, 220 , 420, 623	Cuprite	[56–58]
	B	71, 90, 147 , 177, 199, 220 , 622	Cuprite	[56–58]
	C	73, 90, 94, 148 , 178, 199, 220 , 292, 420, 622	Cuprite	[56–58]
	D	83, 91, 107, 151, 174 , 207, 267 , 351, 430 , 532, 1085, 1365, 1489	Malachite	[59–61]

[56–58], as was also detected with XRD technique as a minor/trace corrosion product. The Raman spectra of layer C in the same samples also displayed similar peaks at 136–137, 220–221 and 627 cm^{-1} corresponding to cuprite.

Raman peaks related to the green layers revealed malachite as the main corrosion product. Intense Raman peaks are observed at 57, 74, 114, 120, 147–148, 169–173, 270–272, 433–436, 1095–1098 and 1491 cm^{-1} respectively [59–61]. It is worth noting that a moderate peak was observed at $\sim 511 \text{ cm}^{-1}$ in the green layer of three samples that may correspond to copper trihydroxychlorides (atacamite or paratacamite) [62, 63].

Figure 10 shows Raman spectra of different corrosion layers present in a completely corroded sample (DD-14) and the arsenical copper sample (DD-18). The red layers of sample DD-14 (layers A and C) show similar Raman spectra with intense peaks at 147–148, 220 and 623 cm^{-1} related to cuprite, while the moderate peak observed at 296 cm^{-1} is related to tenorite [56–58]. Two green layers show the Raman spectra of malachite, including strong peaks at ~ 120 , ~ 149 , ~ 180 , ~ 270 , ~ 440 and 1491 cm^{-1} [59–61], although a moderate peak is also observed at 515 cm^{-1} in layer D that corresponds to atacamite or paratacamite [62, 63].

Discussion

Corrosion morphologies

Accordingly, three corrosion morphologies observed in the Deh Dumen copper alloy objects could be classified as follows:

- M1 morphology is observed in some tin bronze vessels and includes a very thin two-layered internal corrosion crust with some evidence of a very thin external layer. The original surface is the outermost part of the corrosion crust.
- M2 morphology is observed in most of the tin bronze vessels and an vessel's base arsenical copper and includes a four-layered corrosion crust with multiple internal and external corrosion layers, and the limit of the original surface is visibly retained between the layers.
- M3 morphology in which the metal substrate is converted entirely to corrosion products, although the limit of the original surface is also visible between the multi-layered corrosion structure.

The results of observations and analyses showed that all samples were corroded forming a tin-rich corrosion

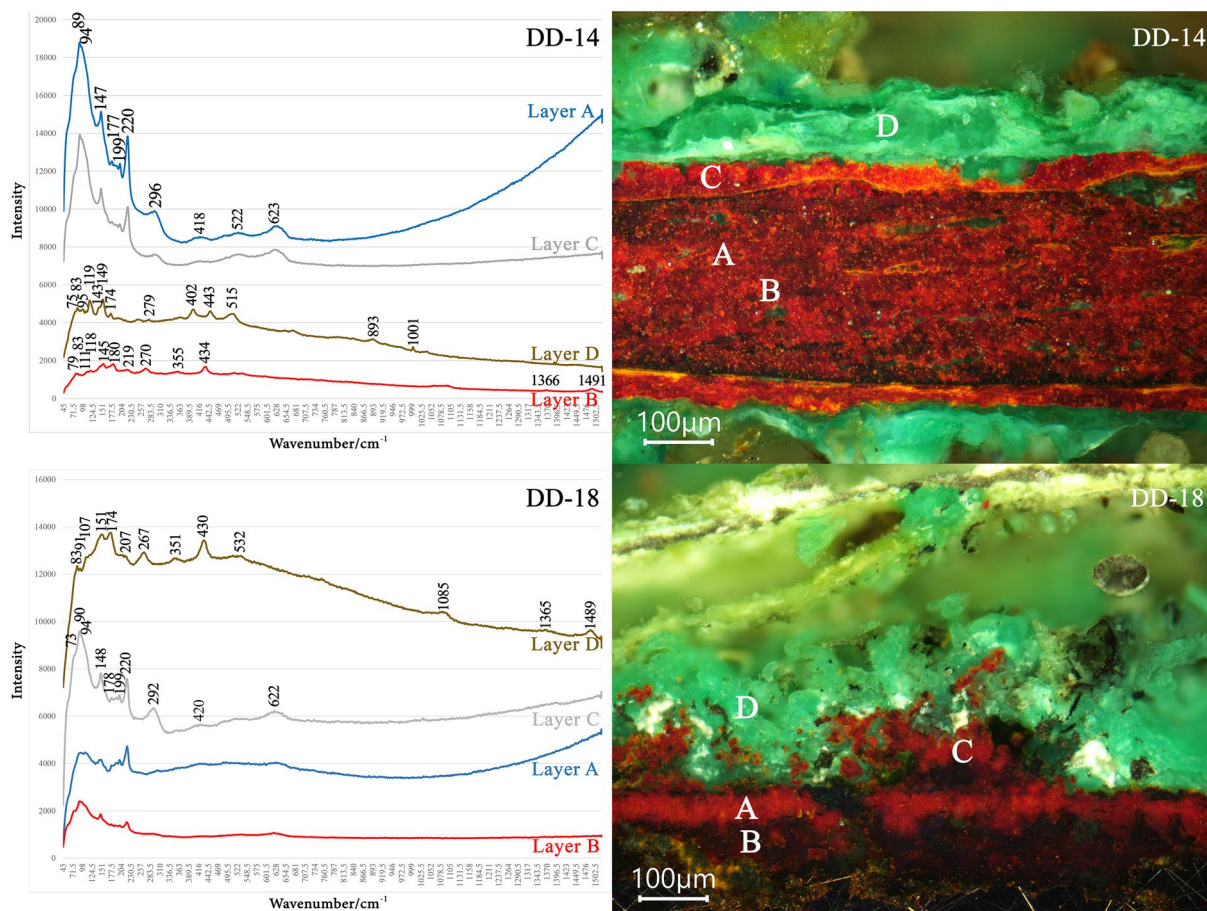


Fig. 10 μ-Raman spectra of different corrosion layers observed in sample DD-14 from M3 morphology and DD-18, the arsenical copper sample

layer (layer A) while there is a variable thickness of red corrosion attack in the interface of layer A and alloy (layer B). This tin-rich internal corrosion layer, known also as noble patina, is typically observed in moderately corroded tin bronze objects and is attributed to copper leaching or decuprification along with internal oxidation of tin during burial time [2, 55, 64, 65]. This process causes to relative enrichment of tin in the corrosion layer in comparison with the alloy [10, 66]. The internal tin-rich surface layer is composed of copper and tin oxides (non-crystalline tin oxide, cuprite and tenorite) and demonstrates a variety of colours influenced by the penetration of soil elements in the layer during corrosion [2, 12, 67]. The tin oxide IV or cassiterite, which forms in the noble patina, is difficult to detect using mineralogical analytical techniques [2, 3, 10]. This is the reason why copper oxides (cuprite and tenorite) were identified as major compounds in the noble patina or internal layer (A) and even the innermost internal layer (B).

Decuprification—dissolution factor

To confirm the identity of this event in the corrosion mechanisms of archaeological bronzes, dissolved copper in a corrosive environment has been calculated in relation to the amount of atomic tin in the alloy using the method for the determination of dissolution factor of alloy components developed by Robbiola et al. [2, 68] and Chiavari et al. [66]. The copper dissolution factor (f_{Cu}) has been calculated for both layers by the following equation:

$$f_{Cu} = 1 - \frac{\left(\frac{X_{Cu,p}}{X_{Sn,p}}\right)}{\left(\frac{X_{Cu,a}}{X_{Sn,a}}\right)}$$

where X_{Sn} and X_{Cu} are respectively amounts of Sn and Cu, and in which **p** indicates the corrosion layers and **a** indicates the alloy, assuming $X_{Sn,a} + X_{Cu,a} = 1$. The copper and tin amounts (X_{Sn} and X_{Cu}) in both layers and alloy have been obtained from results of quantitative SEM–EDS analysis based on atomic percent or atomic fraction (A%), by the average of three analyses. If the Cu/

Sn ratio in the studied layer is equal to the ratio in the alloy, $f_{Cu}=0$, and when all of the Cu has been dissolved and removed, $f_{Cu}=1$. Thus, a higher value of f_{Cu} indicates more copper dissolution during the burial time [68].

For calculating copper dissolution factor, EDS analyses of layer A and B were performed on 18 tin bronze vessels with remnants of uncorroded alloy (three analyses for each layer). Then f_{Cu} was calculated based on atomic percent using the equation presented above. Then the mean f_{Cu} of three analyses from each sample were calculated. Based on the measured means, f_{Cu} in layer A in the investigated samples ranges from 0.56 to 0.93 where $X_{Sn,a} \leq 0.07$. The calculated value for f_{Cu} in all samples is 0.82 with a standard deviation of 0.12 (0.82 ± 0.12), significantly lower than the value calculated by Robbiola et al. [2] and Oudbashi et al. [22]. Calculated f_{Cu} in tin bronze objects buried in Cl-contaminated corrosive environments is not constant and shows lower and variable content, indicating that the dissolution factor of copper is variable and lower in Deh Dumen vessels [69]. The value of f_{Cu} was also calculated for layer B from 0.41 to 0.82 where $X_{Sn,a} \leq 0.07$. The mean calculated value for f_{Cu} in all samples is 0.59 with a standard deviation of 0.12 (0.59 ± 0.12).

Figure 11a shows the scatter plot of f_{Cu} versus $X_{Sn,a}$ calculated in the 18 analysed tin bronze vessels. Figure 11a demonstrates that the factor of copper dissolution is not constant amount for both layers A and B but is variable in the studied samples. Of course, f_{Cu} is consistently higher in layer A than layer B. In fact, there is no apparent relationship between f_{Cu} and $X_{Sn,a}$ in both layers, although the data seem to have a linear behaviour, with a constant slope.

Figure 11b presents the Cu–Sn–O Atomic% ternary diagram based on the concentration of the elements measured with EDS analysis [17]. The plot shows that layer C, the external red layer formed directly over the original surface, is composed of cuprite (Cu_2O) while layer D, the outermost green layer, is mainly composed of copper carbonates (malachite or azurite). It is worth noting that chlorine is detected with EDS as a minor constituent in the green corrosion layer (D), indicating the presence of copper trihydroxychlorides as minor corrosion products combined with malachite. On the other hand, the two internal corrosion layers (A and B) demonstrate a composition between copper oxides (cuprite and tenorite) and tin oxides, revealing that these are formed of a mixture of oxides of two main alloy constituents. Layer A should be mainly composed of tin oxide (probable cassiterite or SnO_2) with some amounts of copper oxide, while layer B tends more to copper oxides.

The elemental EDS map of the cross-section of a heavily corroded vessel (Fig. 6, DD-20) shows that the internal

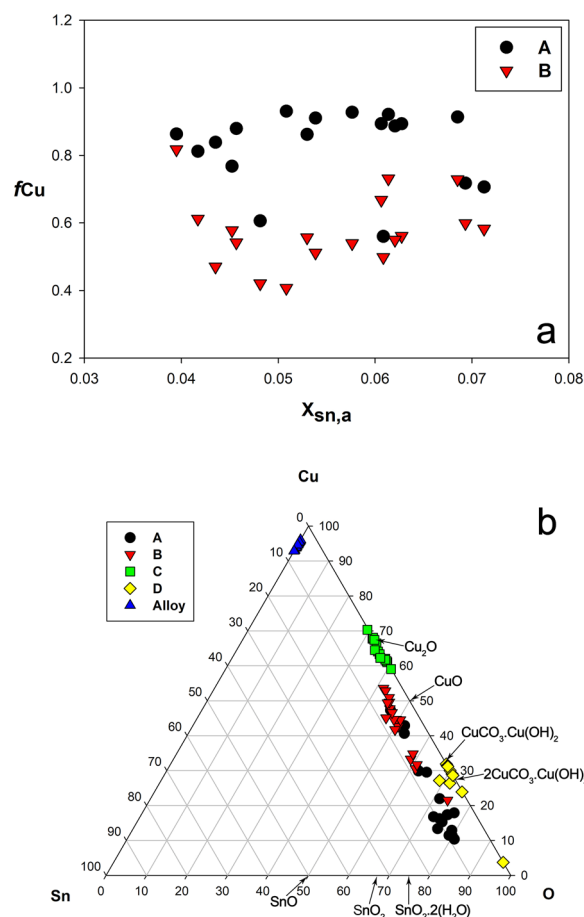


Fig. 11 a Bivariate scatter plot of f_{Cu} versus $X_{Sn,a}$ in alloy-layer A and alloy-layer B [2] based on atomic fraction of Cu and Sn measured with SEM–EDS technique; b Cu–Sn–O ternary diagram based on atomic fraction showing the relationships between Cu, Sn, and O of the external and internal corrosion layers (A, B, C and D) in the corrosion crusts for samples in M1 and M2 morphologies, measured with SEM–EDS technique [17]

corrosion layers contain chlorine as the main constituent. In fact, the internal green layer (layer B in M3 morphology) is composed of copper and chlorine, probably combined with copper carbonates.

Based on results of corrosion studies on the bronze samples, it is clear that the corrosion mechanism occurred in Deh Dumen objects is the selective dissolution of copper, followed by the internal tin oxidation and the reaction of dissolved copper with soil anions with deposition of basic copper carbonates (as well as chlorides) on the surface. This process causes the formation of a thin crust of corrosion products over the original surface. The main corrosion products include copper oxides (cuprite and tenorite), and to a lesser extent, malachite and copper trihydroxychlorides, the presence of which suggests that the burial environment is contaminated with soluble chloride ions. Previous analytical work

on soil of the site corroborated the presence of low concentrations (14–18 µg/kg) of soluble chloride in the burial environment [31]. Presence of chloride in the burial environment usually leads to heavily corroded bronzes that in some cases may cause the complete transformation of metallic bronze to corrosion products [9, 40, 47]. In the Deh Dumen bronzes, evidence of bronze disease is observed due to low concentrations of basic copper chlorides determined in the chemical composition of some corrosion layers.

Figure 12, generated using the online DSS Microstructure and Corrosion of Metals Database (MiCorr) system [70], shows a schematic representation of the three different morphologies observed in the archaeological bronze vessels from Deh Dumen.

It is worth noting that there are four specific layers in all morphologies, including two internal corrosion layers (A and B) and two external corrosion layers (C and D). The limit of the original surface is preserved in all morphologies. The internal layers present a pseudomorphic

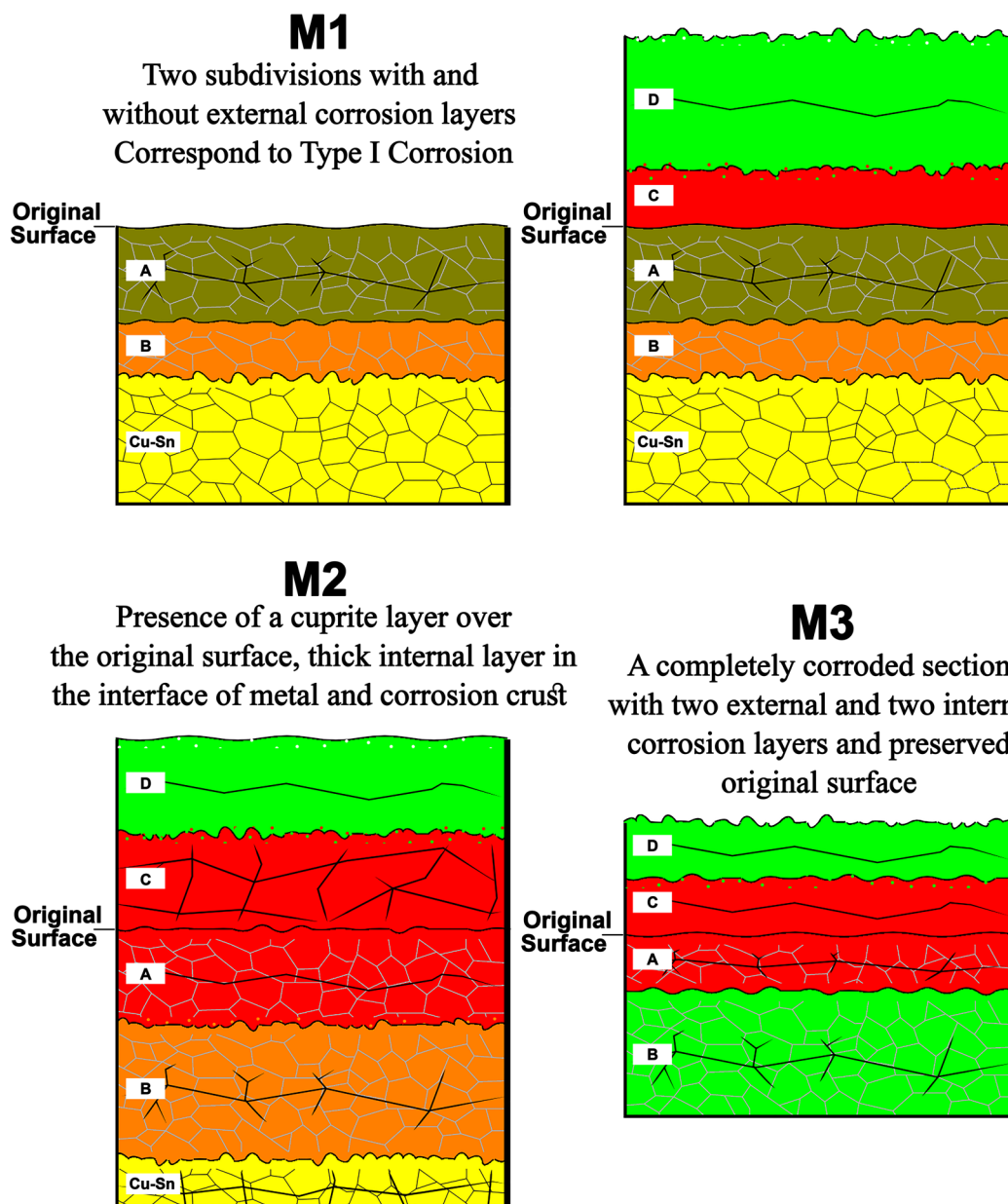


Fig. 12 Schematic representation of the corrosion structure and different morphologies of Deh Dumen bronze artefacts generated by the online DSS Microstructure and Corrosion of Metals Database (MiCorr) system [70]

replacement of the bronze matrix with copper and tin oxides, although some copper carbonates (probably mixed with copper trihydroxychlorides) are formed in the internal layer of M3 objects. The external layers (C and D) are also formed of cuprite and malachite respectively.

M1 morphology observed in some tin bronze vessels is consistent with typical corrosion previously observed in archaeological bronzes. Formation of the two-layered (or three-layered) corrosion on the surface of buried bronzes with preserving the limit of original surface and pseudomorphic replacement could be referred to type I corrosion stated in literature previously. Furthermore, M2 morphology showed no similarities with type I or type II morphologies that are described previously:

1. This is a four-layered corrosion morphology.
2. A thick layer of cuprite formed in the external part, over the original surface.
3. The innermost corrosion layer (B) is very thick.

In fact, this morphology also has some similarities with type II corrosion described by Robbiola et al. [2], in which the limit of the original surface is an area in a thick cuprite layer, but the original surface is not visible. In M2 morphology, the original surface is located under a thick layer of cuprite and is clearly visible. The cross-section of samples also shows that objects of this group are corroded heavily, and a significant fraction of the internal material is converted to corrosion products. The morphology of the heavily corroded groups (samples DD-07, DD-14, DD-20) is similar to the known type II corrosion of bronzes, although the limit of the original surface is also observable in the cross-section. The significant concentration of soluble chloride ions in the burial environment may lead to formation of copper trihydroxychlorides as the main corrosion products, even in the presence of high concentrations of bicarbonate ions in alkaline soils [9, 71]. The formation of malachite as the main corrosion product in Deh Dumen bronzes with some traces of copper trihydroxychlorides could be due to a high concentration of bicarbonate ions and significant concentration of chloride ions in the low alkaline soil [31].

Some objects with M1 morphology from Deh Dumen are similar to previously established type I morphology [2] but others, as well as all M2 objects demonstrated some deviations from it: the presence of an external copper oxide layer formed over the original surface of both, and very thick internal corrosion layers are very clear differences, as it is possible to consider M2 as a new model for long-term corrosion of tin bronze in soil. Also, the M3 morphology (entirely corroded microstructures) is very

similar to previously established type II morphology, but some deviations are also apparent: the original surface is retained well between two layers of red copper oxides and the internal red oxide layer (A) shows the pseudomorphic replacement. Some small deviations from the two previously established corrosion morphologies were observed before in the Iranian tin bronze objects [3, 22] but the Deh Dumen tin bronze vessels exemplify an alternative long-term corrosion of tin bronze in soil as an interstitial morphology, as some characteristics of both type I and II morphologies are combined in one object. Nevertheless, the corrosion morphologies established and developed by Robbiola et al. [2] are very useful yet to interpret the corrosion mechanism and layers in the archaeological bronzes, although development of analytical studies on corrosion of archaeological tin bronze can help us to clarify some unknown aspects of this topic or develop new models for corrosion morphologies.

Conclusions

Investigation on corrosion morphology in twenty tin bronze vessels, as well as one arsenical copper vessel and one arsenical copper vessel's base, from Deh Dumen Bronze Age site, south-western Iran was performed by microscopic and microanalytical techniques. Results identified three corrosion morphologies in the corroded bronze vessels including surface thin multi-layered noble patina (M1), thick multi-layered corrosion crust (M2) and entirely corroded and multi-layered corrosion (M3).

The limit of the original surface is preserved and fully observable in the cross-section of all samples, even in entirely corroded ones. According to the limit of the original surface preserved in all analysed samples, these three corrosion morphologies show a two-layered internal and a two-layered external corrosion crust. The M1 morphology could be compared with the well-known type I corrosion morphology of archaeological bronzes and M3 could be compared with type II. The M2 morphology deviates significantly from the two previously explained morphologies. The main deviations in the Deh Dumen corrosion morphology are the presence of an external cuprite layer formed over the original surface in all identified morphologies, and the preserved original surface even in entirely corroded samples. The thickness of internal corrosion layers in M2 morphology is another deviation, that may be due to significant corrosivity of the soil environment in some burial areas.

Consequently, the corroded tin bronze (and arsenical copper) vessels of Deh Dumen show generally similar morphologies to previously established type I and II corrosion morphologies, but they are different in some important details, that may lead to developing a new corrosion morphology in the future. These variations are

likely due to the presence of chloride anions in the soil environment as well as high water levels due to very low distance between the site and the Khersan river. Generally, this study revealed some new characteristics of long-term corrosion of archaeological tin bronze in the soil environment.

Acknowledgements

The authors are grateful of Dr. Julia G. Bakker-Arkema from the Metropolitan Museum of Art for reading and editing the paper, and Dr. Federico Carò, Dr. Atefeh Shekofteh and Dr. Marco Leona from the Metropolitan Museum of Art for their supports and helps to perform SEM-EDS and Raman spectroscopy analyses.

Author contributions

OO contributed to the sampling and analytical work and interpretation of the analytical data as well as preparing the draft of the manuscript; RN contributed to the sampling and interpretation of the analytical data as well as editing the manuscript; PAH contributed to the sampling and analytical works. All authors read and confirmed the final version of the manuscript.

Funding

This research has been supported by University of Zabol with the Grant Number: UOZ-GR-9618–100.

Availability of data and materials

The datasets used and/or analysed during the current study are available from the corresponding author on reasonable request.

Declarations

Competing interests

The authors declare that they have no competing interests.

Received: 27 November 2023 Accepted: 9 February 2024

Published online: 01 March 2024

References

- Abu-Baker AN, Khalil LA, Al-Gonmeen T. A multi-analytical exploration of the chemical composition, microstructural properties and corrosion inhibiting treatment for an archaeological brass censer from Umm Zuwaytinah, Amman. *Nucl Instrum Meth B*. 2021;502:73–9.
- Robbiola L, Blengino JM, Fiaud C. Morphology and mechanisms of formation of natural patinas on archaeological Cu-Sn alloys. *Corros Sci*. 1998;40(12):2083–111.
- Oudbashi O. Multianalytical study of corrosion layers in some archaeological copper alloy artefacts. *Surf Interface Anal*. 2015;47:1133–47.
- Mortazavi M, Kavosh H, Naghavi S, Khanjari R. Microstructural and analytical study of uncommon corrosion features on archaeological Cu-Sn alloys from Tappeh Graziani in southeastern Iran. *Microsc Microanal*. 2022;28(2):302–16.
- Papadopoulou O, Vassiliou P, Grassini S, Angelini E, Gouda V. Soil-induced corrosion of ancient Roman brass—a case study. *Mater Corros*. 2016;67(2):160–9.
- Liang Z, Jiang K, Zhang T-A. Corrosion behaviour of lead bronze from the Western Zhou Dynasty in an archaeological-soil medium. *Corros Sci*. 2021;191: 109721.
- Ingo GM, Riccucci C, Guida G, Pascucci M, Giuliani C, Messina E, Fierro G, Di Carlo G. Micro-chemical investigation of corrosion products naturally grown on archaeological Cu-based artefacts retrieved from the Mediterranean Sea. *Appl Surf Sci*. 2019;470:695–706.
- Carvalho LDC. Metallic corrosion processes and information from corrosion products. In: Pollard AM, Armitage RA, Makarewicz CA, editors. *Handbook of archaeological sciences*. 2nd ed. Wiley: New Jersey; 2023. p. 1089–102.
- Oudbashi O. A methodological approach to estimate soil corrosivity for archaeological copper alloy artefacts. *Herit Sci*. 2018;6(1):2.
- Piccardo P, Mille B, Robbiola L. Tin and copper oxides in corroded archaeological bronzes. In: Dillmann P, Béranger G, Piccardo P, Matthiesen H, editors. *Corrosion of metallic heritage artefacts: investigation, conservation and prediction for long-term behaviour*. European Federation of Corrosion Publication 48. Cambridge: Woodhead Publishing. 2007. p. 239–62.
- Angelini E, Rosalbino F, Grassini S, Ingo GM, De Caro T. Simulation of corrosion processes of buried archaeological bronze artefacts. In: Dillmann P, Béranger G, Piccardo P, Matthiesen H, editors. *Corrosion of metallic heritage artefacts: investigation, conservation and prediction for long-term behaviour*. European Federation of Corrosion Publication 48. Cambridge: Woodhead Publishing. 2007. p. 203–18.
- Robbiola L, Hurtel LP. Standard nature of the passive layers of buried archaeological bronze; In: MacLeod ID, Pennec SL, Robbiola L, editors. *The example of two Roman half-length portraits*. Metal 95, Proceedings of the International Conference on Metals Conservation. London: James & James. 1997. p. 109–117.
- Robbiola L, Fiaud C, Harch A. Characterization of passive layers of bronze patinas (Cu-Sn alloys) in relation with tin content of the alloy. Modifications of passive films. In: Marcus P, Baroux B, Keddad M, editors. *Proceedings of European Symposium*. European Federation of Corrosion Publication, No. 12. London: The Institute of Materials. 1994. p. 150–154.
- Chase WT. Chinese bronzes: casting, finishing, patination and corrosion. In: Scott DA, Podany J, Considine BB, editors. *Ancient and historic metals: conservation and scientific research*. Los Angeles: Getty Conservation Institute; 1994. p. 85–118.
- Oudbashi O, Emami SM. A note on the corrosion morphology of some Middle Elamite copper alloy artefacts from Haft Tappeh, south-west Iran. *Stud Conserv*. 2010;55:20–5.
- Huarui H, Wenlong B, Dawei L, Jianhua H. Comprehensive research on the layered corrosion of archaeological copper wares: a case study from Qinghai, China. *Stud Conserv*. 2023. <https://doi.org/10.1080/00393630.2023.2236376>.
- Manti P, Watkinson D. Corrosion phenomena and patina on archaeological low-tin wrought bronzes: new data. *J Cult Herit*. 2022;55:158–70.
- Boccaccini F, Riccucci C, Messina E, Pascucci M, Bosi F, Chelazzi D, Guaragnone T, Baglioni P, Ingo GM, Di Carlo G. Reproducing bronze archaeological patinas through intentional burial: a comparison between short- and long-term interactions with soil. *Heliyon*. 2023;9(9):1–13.
- Ghiara G, Maniquet C, Carnasciali MM, Piccardo P. A morphological and chemical classification of bronze corrosion features from an Iron Age hoard (Tintignac, France): the effect of metallurgical factors. *Acta IMEKO*. 2022;11(4):1–10.
- Liu L, Zhong Q, Jiang L, Li P, Xiao L, Gong Y, Zhu Z, Yang J. Metallurgical and corrosion characterization of warring states period bronzes excavated from Pujiang, Chengdu, China. *Herit Sci*. 2022;10:36.
- Bernabale M, Nigro L, Montanari D, De Vito C. Exploring the chemical composition and corrosion patterns of arrowheads used in the Siege of Motya (397 BC) through a multi-analytical approach. *J Cult Herit*. 2021;52:146–52.
- Oudbashi O, Hasanpour A, Davami P. Investigation on corrosion stratigraphy and morphology in some Iron Age bronze alloys vessels by OM, XRD and SEM-EDS methods. *Appl Phys A*. 2016;122:262.
- Ghiara G, Repetto L, Piccardo P. The effect of *Pseudomonas fluorescens* on the corrosion morphology of archaeological tin bronze analogues. *JOM-J Min Met Mat S*. 2019;71:779–83.
- Saraiva AS, Figueiredo E, Aguas H, Silva RJC. Characterisation of archaeological high-tin bronze corrosion structures. *Stud Conserv*. 2022;67(4):222–36.
- Miszkievicz JJ, Stewart TJ, Naseri R, Sołtysiak A. The lifestyles of Bronze Age Zagros highlanders at Deh Dumen, Iran: Insights from mid-shaft femur cross-sectional geometry and histology. *Archaeometry*. 2022;64(5):1270–87.
- Oudbashi O, Naseri R, Cultrone G, Egarter I, Arizzi A. The pottery production from the Deh Dumen Bronze Age graveyard (South-Western Iran): a chemical, mineralogical and physical study. *Herit Sci*. 2021;9:83.

27. Oudbashi O, Renon V, Naseri R. Lead isotope analysis of Bronze Age copper alloy objects from Deh Dumen graveyard, southwestern Iran. *Archaeol Anthropol Sci*. 2023;15:2.
28. Oudbashi O, Naseri R, Malekzadeh K. Technical studies on the bronze age metal artefacts from the graveyard of Deh Dumen, South-Western Iran (Third Millennium BC). *Archaeometry*. 2016;58(6):947–65.
29. Soltysiak A, Naseri R. Human remains from Deh Dumen, Iran, 2013–2016. *Bioarchaeol Near East*. 2017;11:70–5.
30. Soltysiak A, Naseri R, Najafi M. Human remains from Deh Dumen, Iran, 2019. *Bioarchaeol Near East*. 2019;13:142–6.
31. Oudbashi O, Naseri R, Heidarpour B, Ahmadi A. Study on the Corrosion Mechanisms and Morphology of Archaeological Bronze Objects from a Bronze Age Graveyard in Southwestern Iran. In: Chemello C, Brambilla L, Joseph E, editors. *Proceedings of the Interim Meeting of the ICOM-CC Metals Working Group*. Sept. 2–6, 2019, Neuchatel. 2019. p. 150–157.
32. Oudbashi O, Naseri R. Archaeometallurgy of Tin Bronze in the Deh Dumen Bronze Age Graveyard, Southwest of Iran. In: Montero Ruiz I, Perea A, editors. *Proceedings of International Conference AIE4*. Madrid, CSIC; 2015. p. 105–14.
33. Oudbashi O, Wanhill R. Long-term embrittlement of ancient copper and silver. *Heritage*. 2021;4:2287–319.
34. Wanhill RJH, Oudbashi O. Fractography of ancient metallic artifacts, and restoration and conservation aspects. In: *Fractography*. ASM International; 2024. p. 1–19.
35. Quaranta M, Catelli E, Prati S, Sciutto G, Mazzeo R. Chinese archaeological artefacts: microstructure and corrosion behaviour of high-leaded bronzes. *J Cult Herit*. 2014;15(3):283–91.
36. Taube M, Davenport AJ, King AH, Chase WT. Selective dissolution in copper-tin alloys: Formation of corrosion-resistant patina on ancient Chinese bronze mirrors. *MRS Online Proc Libr*. 1996;432:283–8.
37. Ingo GM, De Caro T, Riccucci C, Khosroff S. Uncommon corrosion phenomena of archaeological bronze alloys. *Appl Phys A*. 2006;83:581–8.
38. Robbiola L, Queixalós I, Hurltel LP, Pernot M, Volfovsky C. Etude de la corrosion de bronzes archéologiques du Fort-Harrouard: alteration externe et mécanisme d'altération stratifiée. *Stud, Conserv*. 1988;33(4):205–15.
39. Bertholon R. Characterisation and location of original surface of corroded metallic archaeological objects. *Surf Eng*. 2001;17(3):241–5.
40. Scott DA. *Copper and bronze in art: corrosion, colorants, conservation*. Los Angeles, CA: Getty Conservation Institute; 2002.
41. Selwyn LS. *Metals and corrosion: a handbook for the conservation professional*. Ottawa: Canadian Conservation Institute; 2004.
42. Luo W, Jin R, Qin Y, Huang F, Wang C. Analysis of the corrosion products of the ancient bronzes excavated from Qiaojayuan Tombs. *Appl Phys Res*. 2010;2:156–69.
43. Abu-Baker AN. A technical examination of the corrosion and microstructural features of copper alloy artifacts from the Byzantine Period at Khirbet Yajuz, Jordan. *Metallogr Microstruct Anal*. 2023;12(2):276–88.
44. Festa G, Caroppi PA, Filabozzi A, Andreani C, Arancio ML, Triolo R, Lo Celso F, Benfante V, Imberti S. Composition and corrosion phases of Etruscan Bronzes from Villanovan Age. *Meas Sci Technol*. 2008;19(3): 034004.
45. McNeil MB, Little BJ. Corrosion mechanisms for copper and silver objects in near-surface environments. *J Am Inst Conserv*. 1992;31:355–66.
46. Vink BW. Stability relations of malachite and azurite. *Mineral Mag*. 1986;50:41–7.
47. Selwyn LS. Corrosion of metal artifacts in buried environments. *ASM Handbook Volume 13C, Corrosion: Environments and Industries*, ASM International. 2006. p. 306–322.
48. Scott DA. A review of copper chlorides and related salts in bronze corrosion and as painting pigments. *Stud Conserv*. 2000;45(1):39–53.
49. Scott DA. Bronze disease: a review of some chemical problems and the role of relative humidity. *J Am Inst Conserv*. 1990;29(2):193–206.
50. Fischer WR, Wagner BD, Siedlerek H, Fußinger B. The influence of chloride ions and light on the corrosion behaviour of copper alloys in aqueous environment with special regards to bronze disease. *Metal 95*, In: MacLeod ID, Pennec SL, Robbiola L, editors. *Proceedings of the International Conference on Metals Conservation*. Semur en Auxois, 25–28 Sept. 1995. London: James & James. 1997. p. 89–94.
51. Fitzgerald KP, Nairn J, Skennerton G, Atrens A. Atmospheric corrosion of copper and the colour, structure and composition of natural patinas on copper. *Corros Sci*. 2006;48:480–2509.
52. Fitzgerald KP, Nairn J, Atrens A. The chemistry of copper patination. *Corros Sci*. 1998;40:2029–50.
53. Muras V, Scott DA. The occurrence of brochantite on archaeological bronzes: a case study from Lofkënd, Albania. *Stud Conserv*. 2018;63:113–25.
54. Bernard MC, Joiret S. Understanding corrosion of ancient metals for the conservation of cultural heritage. *Electrochim Acta*. 2009;54(22):5199–205.
55. Ospitali F, Chiavari C, Martini C, Bernardi E, Passarini F, Robbiola L. The characterization of Sn-based corrosion products in ancient bronzes: a Raman approach. *J Raman Spectrosc*. 2012;43(11):1596–603.
56. Colomban P, Tournié A, Maucuer M, Meynard P. On-site Raman and XRF analysis of Japanese/Chinese bronze/brass patina—the search for specific Raman signatures. *J Raman Spectrosc*. 2012;43(6):799–808.
57. Bongiorno V, Campodonico S, Caffara R, Piccardo P, Carnasciali MM. Micro-Raman spectroscopy for the characterization of artistic patinas produced on copper-based alloy. *J Raman Spectrosc*. 2012;43:1617–22.
58. Serghini-Idrissi M, Bernard MC, Harrif FZ, Joiret S, Rahmoun K, Srhiri A, Takenouti H, Vivier V, Ziani M. Electrochemical and spectroscopic characterizations of patinas formed on an archaeological bronze coin. *Electrochim Acta*. 2005;50(24):4699–709.
59. Buzgar N, Apopei AI. The Raman study of certain carbonates. *Geologie*. 2009;L/2:97–112.
60. Frost RL, Martens WN, Rintoul L, Mahmutagic E, Klopogge JT. Raman spectroscopic study of azurite and malachite at 298 and 77 K. *J Raman Spectrosc*. 2002;33(4):252–9. <https://doi.org/10.1002/jrs.848>.
61. Yu BS, Fang JN, Huang EP. Characteristics of the Raman spectra of archaeological Malachites. *J Raman Spectrosc*. 2013;44(4):630–6.
62. McCann LI, Trentelman K, Possley T, Golding B. Corrosion of ancient Chinese bronze money trees studied by Raman microscopy. *J Raman Spectrosc*. 1999;30:121–32.
63. Frost RL, Martens W, Klopogge JT, Williams PA. Raman spectroscopy of the basic copper chloride minerals atacamite and paratacamite: implications for the study of copper, brass and bronze objects of archaeological significance. *J Raman Spectrosc*. 2002;33(10):801–6. <https://doi.org/10.1002/jrs.921>.
64. Robbiola L, Portier R. A global approach to the authentication of ancient bronzes based on the characterization of the alloy–patina–environment system. *J Cult Herit*. 2006;7(1):1–12.
65. Sidot E, Souissi N, Bousselmi L, Triki E, Robbiola L. Study of the corrosion behaviour of Cu–10Sn bronze in aerated Na₂SO₄ aqueous solution. *Corros Sci*. 2006;48(8):2241–57.
66. Chiavari C, Rahmouni K, Takenouti H, Joiret S, Vermaut P, Robbiola L. Composition and electrochemical properties of natural patinas of outdoor bronze monuments. *Electrochim Acta*. 2007;52:7760–9.
67. Robbiola L, Vilbert D, Lejars T, Bourgarit D, Mille B. Characterization of a buried archaeological bronze from the Celtic tomb n 1002 of La Fosse Cotheter (Roissy-en-France). *Metals 2001: Proceedings of the ICOM Committee for Conservation Metals Working Group*, 2004. p. 237–242.
68. Robbiola L, Tran TTM, Dubot P, Majerus O, Rahmouni K. Characterisation of anodic layers on Cu–10Sn bronze (RDE) in aerated NaCl solution. *Corros Sci*. 2008;50(8):2205–15.
69. Bernabale M, Cognigni F, Mura F, Nigro L, Montanari D, Rossi M, De Vito C. 3D imaging of micro-segregation and corrosion behavior of alloying elements in archaeological artefacts from Motya (Sicily, Italy). *Corros Sci*. 2023;211: 110900. <https://micorr.org/>.
70. <https://micorr.org/>.
71. MacLeod ID, Paterakis AB. Integration of laboratory and field measurements on soil and bronze artifacts: facilitating conservation treatment and management of archaeological collections. *J Am Ins Conserv*. 2023;62(2):81–100.

Publisher's Note

Springer Nature remains neutral with regard to jurisdictional claims in published maps and institutional affiliations.